

Effect of Ion Pair on Contact Angle for Phosphonium Ionic Liquids

Ting Liu, Md Hafizur Rahman, Pradeep L. Menezes, and Ashlie Martini*



Cite This: <https://doi.org/10.1021/acs.jpcb.2c01989>



Read Online

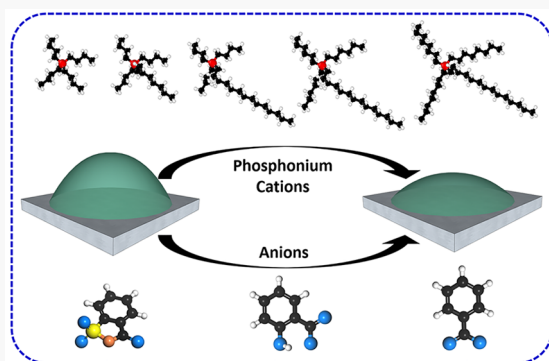
ACCESS |

Metrics & More

Article Recommendations

Supporting Information

ABSTRACT: The wettability of ionic liquids (ILs) is relevant to their use in various applications. However, a mechanistic understanding of how the cation–anion pair affects wettability is still evolving. Here, focusing on phosphonium ILs, wettability was characterized in terms of contact angle using experiments and classical molecular dynamics simulations. Both experiments and simulations showed that the contact angle was affected by the anion and increased as benzoate < salicylate < saccharinate. Further, the simulations showed that the contact angle decreased with increasing cation alkyl chain length for these anions paired with five different tetra-alkyl-phosphonium cations. The trends were explained in terms of adhesive and cohesive energies in the simulations and then correlated to the atomic scale differences between the anions and the cations.



INTRODUCTION

Ionic liquids (ILs) are salts in the liquid state below 100°C or even at room temperature (25°C).¹ ILs have a unique combination of physicochemical properties, including low vapor pressure or nonvolatility, wide range of solubility, tunable acidity and basicity, high thermal stability, high ion conductivity, and large electrochemical window.^{1,2} These properties enable ILs to be used as organic solvents, mineral acids, bases, catalysts, and many more for a diverse range of applications.^{1–6}

ILs comprise positively charged cations and negatively charged anions. A variety of anions, both organic and inorganic, are used in application-relevant ILs, but cations are usually organic species such as ammonium, phosphonium, imidazolium, or pyridinium.^{1,7} Among these ILs, phosphonium ILs have been reported to have low wear and friction as lubricants,^{8,9} high chemical and thermal stability,^{10,11} as well as superior resistance to corrosion.^{12–14} Importantly, many halogen-free phosphonium ILs are considered environmentally friendly^{15–17} since they are biodegradable and can be extracted from biobased feedstock.^{5,18–20} Therefore, phosphonium ILs are used as lubricants/lubricant additives,^{21–26} battery electrolytes,^{27–29} heat transfer fluids,^{30,31} solvents for coating materials,^{32,33} and additives in polymeric materials.^{34–38}

In many applications, phosphonium ILs are in contact with a solid surface and form a solid–liquid interface. Therefore, the adsorption and spreading of phosphonium ILs on solid surfaces, i.e., wettability, plays an important role in their performance.^{39–41} Wettability is controlled by the balance between the intermolecular adhesion (liquid–solid) and cohesion (liquid–liquid) interactions.⁴² For phosphonium ILs used as lubricants, wettability is important because it affects the fluid's ability to spread and protect solid

surfaces.^{40,43} Wetting is also important for phosphonium ILs used as electrolytes since the utilization rate of electrode surface area and the energy density of supercapacitors can be improved by increasing wettability.⁴⁴

Usually wettability is quantified as the contact angle between a liquid droplet and a solid surface.⁴⁵ Strong adhesion to the substrate surface and weak cohesion within the liquid lead to a high degree of wetting with small contact angles, while a combination of weak adhesion and strong cohesion results in large contact angles and poor wetting. When a droplet is placed on a surface, there is initially transient evolution of the contact angle as the liquid droplet is wetting the surface and then the contact angle reaches steady state. Both the transient and the steady-state contact angles are used to characterize wetting behavior. Usually, a steady-state contact angle less than 90° indicates good wettability.⁴⁶ The wetting time, the time required for the contact angle to reach steady state, can be used to determine the relative strengths of adhesion and cohesion. Longer wetting times indicate adhesion domination, whereas shorter wetting times indicate the dominance of cohesion.⁴⁷ These properties can be measured experimentally using a goniometer as well as with molecular dynamics (MD) simulations that give an atomistic view of contact angle mechanisms.

Experimental studies have reported the contact angle of neat phosphonium ILs measured on a variety of surfaces and at a

Received: March 22, 2022

Revised: May 23, 2022

range of temperatures. All reported good wettability with contact angles less than 90°.^{39,40,47–51} Some studies have compared contact angles on different substrates and shown that wettability is better on materials with a high surface free energy, e.g., lower contact angle on steel than PTFE⁴⁹, and lower contact angle on TiN than steel, CrN, and ZrN.⁴⁰ Temperature has also been shown to affect the contact angle. However, while the contact angle of some ILs decreases with increasing temperature,³⁹ other ILs exhibit the opposite trend.⁴⁷ Lastly, the wettability of phosphonium ILs in solution has been measured experimentally, and it has been reported that contact angles of IL solutions could be smaller or larger than those of the neat ILs depending on the solvent and substrate material.^{22,52}

MD simulations have been used to complement experiments by exploring the atomistic origins of IL wettability.^{53–58} However, currently there are few simulation studies focused on the wettability of phosphonium ILs. Simulations showed that the steady-state contact angle of [P4,4,4,4][Cpy] on silanol and silane surfaces was less than 90°, indicating strong liquid–surface adhesion, but the contact angle was slightly larger on the silane surface.⁵⁹ The steady-state contact angle of [P2,2,2,5][Tf₂N] nanodroplets on platinum surfaces at 298 K was calculated in simulations. The results showed that the contact angle on Pt(100) was higher than that on Pt(111), demonstrating that the crystallographic nature of the surface can affect spreading. The simulations also compared two different ILs and found that the contact angle of [P2,2,2,5][Tf₂N] nanodroplets was lower than that of [N2,2,2,5][Tf₂N] on both Pt surfaces.⁵⁸

IL properties, including wettability, are significantly affected by the chemistry and structure of the cation and anion combination.^{5,60} No previous studies specifically for phosphonium ILs focused on the effect of the cation. However, some studies for other ILs reported that longer cation alkyl chains corresponded to lower contact angle. For example, the contact angle of [Tf₂N] anion-based ILs with different cations was experimentally found to be lower for longer alkyl chains, with contact angles increasing as [C₁₀C₁im] < [C₄C₁im] < [C₂C₁im].⁵⁴ This trend was consistent with simulation results that showed that the radial distribution function (RDF) peaks were sharper and higher for longer chains, indicating better ordering near the surface.⁵⁴ In a simulation study, the contact angle of [BF₄]-based ILs on the graphite surface was lower for the [PrMIM] cation with a longer alkyl chain compared to the [DMIM] cation with a shorter alkyl chain. The interaction energy between graphite and [PrMIM][BF₄] was found to be higher than that for [DMIM][BF₄], which implied that the longer [PrMIM] cations had a stronger affinity toward the graphite surface, leading to a lower contact angle.⁵⁵ Lastly, simulations showed that contact angles of ILs with [BMIM] with long alkyl chains were lower than those of [EMIM] ILs with short chains for anions including [Cl], [Br], [BF₄], [PF₆], and [Tf₂N] on bismuth telluride surfaces.⁵⁷

For the effect of the anion, it was reported that, for [P6,6,6,14] cations, the contact angle increased as [p-TsO] < [Tf₂N] < [Cl] < [DCA] < [BF₄] on PTFE surfaces. The lower contact angle of [p-TsO] was attributed to the planarity and electron density of the aromatic ring.⁵⁰ An experimental study reported that the contact angle increased as [BEHP] < [(iC₈)₂PO₂] < [Cl] < [DCA] on AISI 52100 steel, CrN, and ZrN surfaces for the same [P6,6,6,14] cation. This trend was attributed to the inverse relationship between anion size and

surface tension.⁴⁰ The effect of anion size was also observed in simulations of nonphosphonium ILs that showed that larger anions had better wetting on bismuth telluride surfaces and the contact angle decreased as [Cl] > [Br] > [BF₄] > [PF₆] > [Tf₂N] for imidazolium-based ([BMIM] and [EMIM]) ionic liquids. This trend was attributed to the higher cohesion energy for the larger anions.⁵⁷

The results reported so far have shown that the cation and anion can affect the wettability, but there has been no systematic study of these effects for phosphonium ILs nor the underlying mechanisms. Here, we explored the relationship between the phosphonium cation–anion pairs and the contact angle. In particular, the effect of different anions (especially with similar chemistries) for the same cation, and the effect of alkyl chain length in tetra-alkyl-phosphonium cations for the same anion were studied. Although the wetting behavior depends on the surface material and morphology as well,⁵⁸ here we focused on the effects of the cation and anion. First, the wettability of three ionic liquids with benzoate [Benz], salicylate [Sali], and saccharinate [Sacc] anions paired with the [P6,6,6,14] cation was experimentally measured on 52100 stainless steel. Then the contact angle for these phosphonium ILs on a model iron surface was calculated using MD simulations to confirm the trends observed in experiments. The simulations were extended to characterize the effect of the cation for ILs with [P4,4,4,4], [P4,4,4,8], [P4,4,4,14], [P6,6,6,14], and [P8,8,8,14] cations. Finally, the origins of the observed cation and anion trends were explored in terms of the strength of the adhesion and cohesion interactions.

■ METHODS

Experiments. Three ILs were synthesized through ion exchange reactions using [P6,6,6,14] chloride and either sodium saccharinate, sodium salicylate, or sodium benzoate following the process described previously by Reeves et al.⁶¹ and other researchers^{62,63} to yield [P6,6,6,14][Sacc], [P6,6,6,14][Sali], and [P6,6,6,14][Benz]. A mirror-finished AISI 52100 stainless steel surface was prepared using silicon carbide polishing papers of 120, 240, 400, 600, and 1000 grit size followed by diamond suspensions of 6, 3, and 1 μm. The average surface roughness ($R_a = 17.9 \pm 4.9$ nm) was measured using an optical profilometer (Rtec, CA, USA) with 10× magnification using white light interferometry.

The contact angle measurements of the three phosphonium ILs were carried out using a goniometer (Rame-Hart model 260, NJ, USA). A 5 μL sessile droplet of each liquid was deposited on the surface using a microsyringe assembly with a SS 304, straight, 22 gauge needle, and the droplet was imaged using a camera with a 750 FPS superspeed U2 series upgrade kit, all manufactured by Rame-Hart. The contact angle was calculated as the angle between the line along the stainless steel surface and the tangential line to the droplet surface. The contact angles on either side of the sessile droplet were recorded at a 1 s interval using Dropimage software, and the average of the contact angle on the two sides of the droplet (θ) was tracked over time. Each test was repeated three times.

Molecular Dynamics Simulation. Since the cation alkyl chain length affects the contact angle, the simulations were extended beyond the IL systems studied experimentally to include five different cations [P4,4,4,4], [P4,4,4,8], [P4,4,4,14], [P6,6,6,14], and [P8,8,8,14] in combination with three anions [Benz], [Sali], and [Sacc]. Snapshots of the individual ions are shown in Figure 1. Each simulation had one IL droplet on a

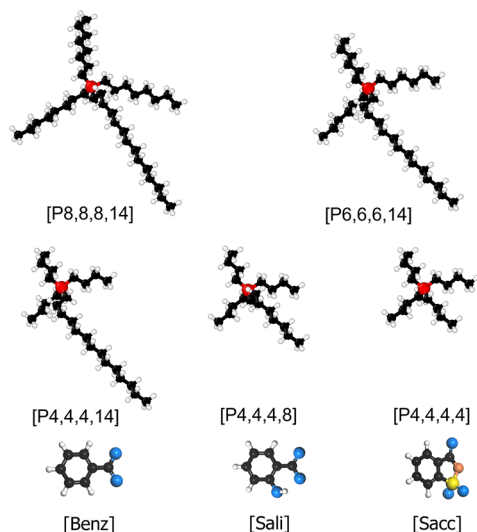


Figure 1. Snapshots of the molecular models of the five cations and three anions used in the simulations of phosphonium ILs. Sphere colors correspond to atom type: white, H; black, C; red, P; blue, O; orange, N; yellow, S.

250 × 250 Å square surface comprising five layers of Fe atoms arranged in a body-centered-cubic lattice with a (111) orientation with the bottom layer fixed, as shown in Figure 2.

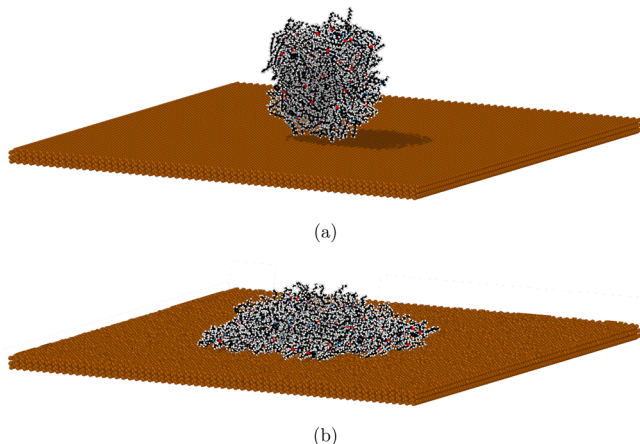


Figure 2. Perspective view snapshots (a) of the model IL droplet contacting the surface and (b) after 10 ns of relaxation for [P6,6,6,14][Benz].

The interatomic interactions within and between the ILs were described by the OPLS-AA force field⁶⁴ based on LigParGen.⁶⁵ Interactions within the iron substrate were modeled using the Lennard-Jones (LJ) potential with $\epsilon = 0.2007$ eV and $\sigma = 2.4193$ Å.⁶⁶ Interactions between the substrate and the ILs were modeled using the LJ potential combining the Fe parameters with the LJ parameters of OPLS-AA using geometric mixing rules.⁶⁷

It has been reported that the contact angle increases linearly with droplet size until it converges to a constant value after a critical number of ions or droplet radius is reached.^{68,69} In previous simulations, the contact angle was found to converge for [BMIM][BF₄] on graphene with at least 100 ion pairs⁶⁹ or an initial cubic box size of 50 Å⁵⁵ and for [EMIM][BF₄] on silicon with a droplet radius of at least 20 Å.⁷⁰ On the basis of these, all model phosphonium IL systems here were created

using PACKMOL⁷¹ with at least 100 ion pairs, corresponding to the liquid in a 50 Å cubic volume. The IL cube was initially placed 10 Å above the iron surface. All MD simulations were performed using the open-source Large Atomic/Molecular Massively Parallel Simulation (LAMMPS) package⁷² with a time step of 1 fs.

First, energy minimization was performed using the conjugate gradient algorithm until reaching a stopping tolerance of 1.0×10^{-6} for energy and 1.0×10^{-8} for force. After energy minimization, the IL was partially relaxed as the temperature was increased from 1 to 298 K over 1 ns in a canonical ensemble (NVT). The Nosé-Hoover thermostat⁷³ was used to control the temperature of the system, and the velocity-Verlet algorithm⁷⁴ was applied to solve the equations of motion. This relaxation procedure ensured cohesion in the ionic liquid and droplet formation. During this relaxation stage, the cube IL droplet became a more physically realistic spherical shape and came into contact with the substrate surface, as shown in Figure 2a. Then, the production simulation was run at a temperature of 298 K for another 10 ns. The droplet spread on the surface starting from the initial point of contact between the droplet and the surface, finally reaching a steady-state shape like that shown in Figure 2b. Each simulation was run three times from the same initial atomic configuration with different initial velocity distributions.

In previous simulation studies,^{57–59} the contact angle was determined using a simple two-dimension method as the angle between the horizontal line at the liquid–solid interface and the line tangent to the droplet surface at the liquid–solid–vapor three-phase contact point. This calculation has also been performed using more complicated three-dimensional algorithms.^{70,75,76} However, the tangent line is difficult to define for the relatively large and branched ions here. Therefore, the contact angle was determined by the equation $\theta = \tan^{-1}(h/r)$, where r is the radius of the liquid–solid contact circle and h is the height of the apex;^{53,77} details of the contact angle calculation are given in Figure S1. After the potential energy reached a steady state, the contact angle was calculated by averaging 20 trajectories (time steps) during the last 1 ns of the simulation.

Throughout the simulation, the adhesive and cohesive energies were calculated from the sum of the energies between individual atom pairs. The adhesion energy was calculated as the sum of the energy between atoms in the anion or cation and the Fe atoms in the substrate; cohesion energy was calculated as the total interaction energy between atoms in the anion and cation. These summed energies were averaged over the last 1 ns of the production simulations, consistent with the contact angle calculation. A negative adhesive or cohesive energy corresponds to net attraction.

RESULTS AND DISCUSSION

Comparison of Experiments and Simulations. The ILs measured experimentally comprised [P6,6,6,14] with three different anions. As shown in Figure 3a, the contact angle of all three ILs decreased rapidly to approach a steady-state value. At steady state, the contact angles of [P6,6,6,14][Sacc], [P6,6,6,14][Sali], and [P6,6,6,14][Benz] were 14.2°, 6.89°, and 4.10°, respectively. The small contact angles measured here are consistent with previous studies of [P6,6,6,14][Tf₂N] ILs on a stainless steel surface,^{47,51} which also reported contact angles less than 20°. Generally, the results indicate that all three phosphonium ILs have good wettability on stainless steel.

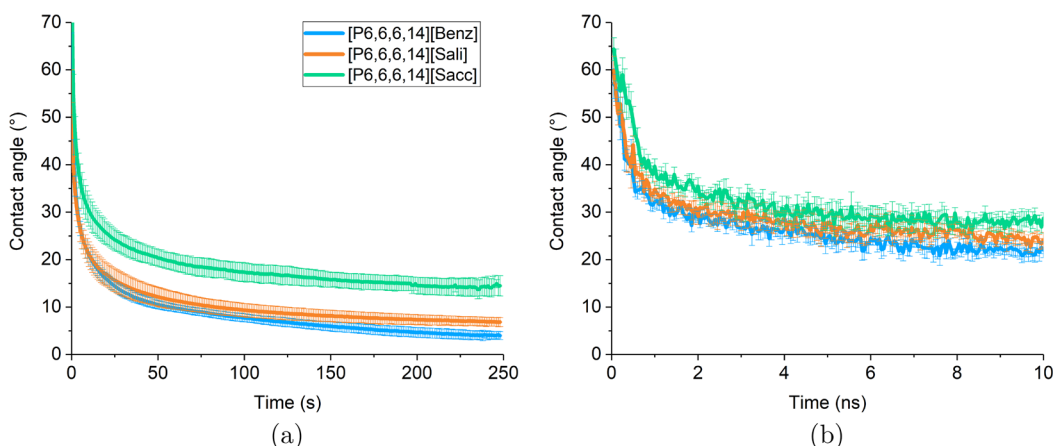


Figure 3. (a) Contact angle as a function of time for $[P6,6,6,14][Benz]$, $[P6,6,6,14][Sali]$, and $[P6,6,6,14][Sacc]$ from (a) experimental measurements on a polished AISI 52100 steel surface with error bars reflecting the standard deviation across four independent measurements, and (b) simulation calculations on the Fe (111) surface with error bars reflecting the standard deviation across three independent MD simulations.

Among the three ILs, $[P6,6,6,14][Sacc]$ had the largest contact angle, more than twice that of $[P6,6,6,14][Sali]$ and $[P6,6,6,14][Benz]$, over the entire spreading time. For $[P6,6,6,14][Sali]$ and $[P6,6,6,14][Benz]$, the contact angles were not statistically different during the transient phase, but, at steady state, $[P6,6,6,14][Sali]$ had a larger contact angle. These results indicate that the anion can affect the contact angle, as observed in previous studies.^{39,47–49,51,78}

MD simulations were carried out for the three $[P6,6,6,14]$ -based ILs characterized experimentally. As shown in Figure 3b, the contact angle of all three ILs gradually decreased during the 10 ns simulation. The average contact angles over the last 1 ns of the simulation for $[P6,6,6,14][Sacc]$, $[P6,6,6,14][Sali]$, and $[P6,6,6,14][Benz]$ were 28.1° , 24.3° , and 21.8° , respectively. The magnitudes of the simulation contact angles were larger than those in experiment due to the limited size and time scales of the simulations. The time scale of the experiments in Figure 3a is seconds, while that of the simulations in Figure 3b is nanoseconds, so the results cannot be directly compared. However, despite their differences, in both simulations and experiments, $[P6,6,6,14][Sacc]$ had the largest steady-state contact angle and $[P6,6,6,14][Benz]$ had the smallest.

As mentioned in the *Introduction*, both the cation and the anion can affect the wettability. The simulations were used to explore this further by comparing the contact angle for ILs with the three anions characterized above combined with five different cations. The effects of the cations and anions were analyzed separately with trends investigated in terms of adhesive and cohesive energies.

Effect of Cations. The steady-state contact angle is plotted with respect to the cation in Figure 4. It is observed that the steady-state contact angles decreased with increasing alkyl chain length for all three anions. This trend was also reported in previous studies for imidazolium cations.^{54,55,57} Another observation in Figure 4 is that the contact angle decreased with increasing cation size, regardless of whether the size increase was in one chain (compare $[P4,4,4,4]$, $[P4,4,4,8]$, and $[P4,4,4,14]$) or multiple chains ($[P4,4,4,14]$, $[P6,6,6,14]$, and $[P8,8,8,14]$). The overall trend may be due to the longer chains increasing adhesion or decreasing cohesion or both.

The total Fe–IL adhesion energy, reported in Figure 5a, increased (became more negative) with increasing cation chain

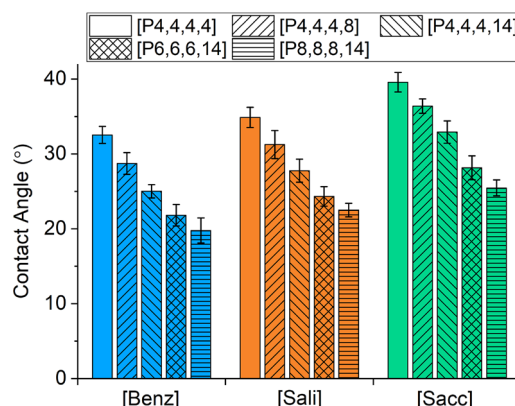


Figure 4. Comparison of the steady-state contact angle for cations with different alkyl chain lengths paired with three different anions. Error bars reflect the standard deviation among three independent MD simulations. Data is grouped by anion to highlight the effect of the cation.

length, consistent with the trend of decreasing contact angle. The adhesive energy was separated into contributions from the cation and anion, as shown in Figure 5b. The Fe–cation adhesive energy increased with chain length, while the Fe–anion energy decreased with chain length. However, the magnitude of the cation adhesion was much larger than that for the anion, so the cation trend dominated the overall adhesion with the surface. The Fe–cation interaction energy was further broken down by atom type (Figure 5b), and it was found that the C atoms contribute most to the total adhesion. Therefore, the increasing adhesive energy trend can be attributed to the fact that there are more C atoms present in the longer chains.

The cohesion between ions was also analyzed. It was found that the only attractive interionic interactions were between the P atoms in the cation and the atoms in the anions (Figure S3). The cohesive energy between the cation P atoms and the anions, shown in Figure 6a, decreased (becomes less negative) with increasing chain length. The trend could be due to the interference of the longer chains that separated the anion and the cation, thereby decreasing cohesion. This hypothesis was confirmed by calculating the average distance between the cation P atom and the center-of-mass (COM) of the nearest anion. As shown in Figure 6b, the cation–anion distance

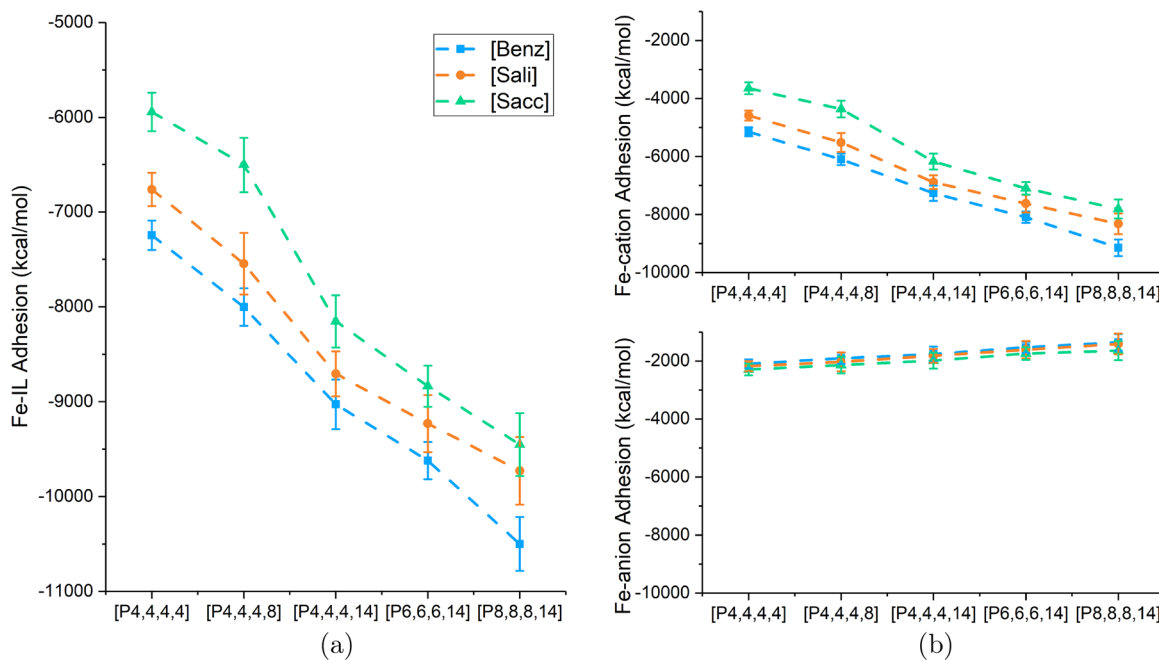


Figure 5. Adhesive interaction energy between the surface and the ILs and (b) separated into the cation (top) and anion (bottom) contributions plotted as a function of increasing alkyl chain length for the three anions.

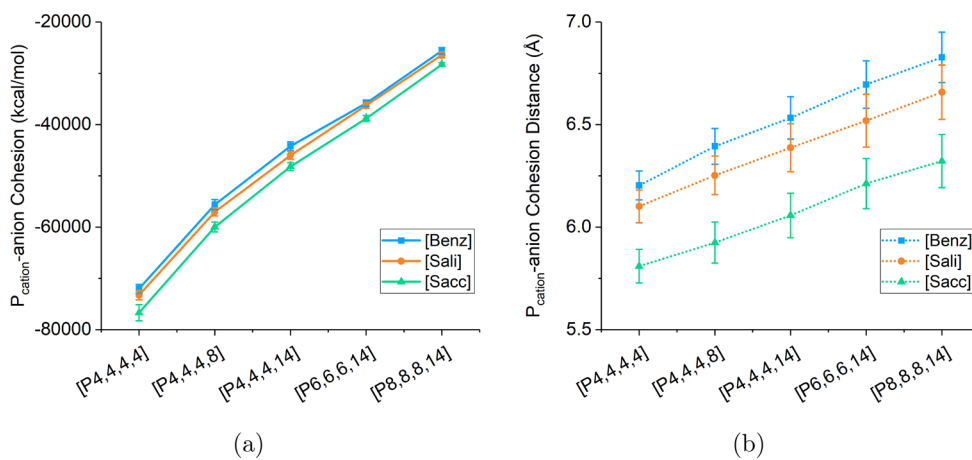


Figure 6. (a) Cohesive energy between P atoms in the cations and all atoms in the anions, and (b) average distance between cation P atoms and the COM of the anions plotted as a function of increasing alkyl chain length for the three anions.

increased with alkyl chain length, consistent with the decreasing cohesive energy and the corresponding lower contact angle.

Effect of Anions. The steady-state contact angles are plotted with respect to the anion in Figure 7. For all five cations, the contact angle increased as [Benz] < [Sali] < [Sacc]. It has been proposed that larger anions will have lower contact angles.⁴⁰ Anions with aromatic rings like [p-TsO] have also been reported to have lower contact angles than anions without aromatic rings like [BF₄], [DCA], [Cl], and [Tf₂N] because of the planarity and delocalized electron density of the ring.⁵⁰ However, [Benz], [Sali], and [Sacc] are all aromatic ring-based anions with similar size, so the difference in their contact angles should be attributed to other mechanisms. First, the adhesion and cohesion were analyzed following the approach used to explain the cation trends.

The total Fe-IL adhesion energy, plotted vs anion in Figure 8a, was largest for [Benz] and smallest for [Sacc]. This trend is

consistent with the observation that [Benz] has the lowest contact angle while [Sacc] has the largest contact angle. To explain how the anions affect the total adhesion, the Fe-anion and Fe-cation adhesive energies were analyzed separately.

As shown in Figure 8b, the Fe-anion adhesive energy increases as [Benz] < [Sali] < [Sacc]. This may be due to the fact that [Sacc] has the most atoms, and, as shown in Figure S4, the biggest contribution to adhesion in [Sacc] is the S atom that is not present in the other two anions. Similarly, for [Sali], there is one more O atom in the hydroxyl group than [Benz] which could contribute to the higher interaction energy observed for [Sali]. However, this difference in Fe-anion energy is very small compared to the difference between the anions in terms of Fe-cation adhesion. The Fe-cation adhesion is largest for [Benz] and smallest for [Sacc], consistent with the contact angles. Therefore, the anion contact angle trend can be attributed to the indirect effect of

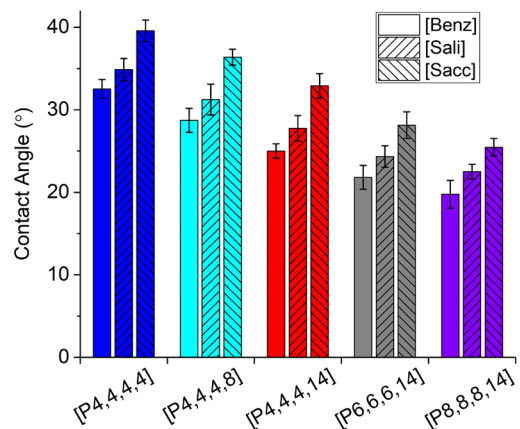


Figure 7. Comparison of the steady-state contact angle for anions [Benz], [Sali], and [Sacc] paired with five different cations. Error bars reflect standard deviation among three independent MD simulations. Note that this is the same data as in Figure 4 but shown here with the data grouped by cation to highlight the effect of anion.

the anion on interactions between the cations and the substrate.

Since the Fe–anion energy is not very different for the three anions, their effect on cation adhesion may be due to the orientation of the anions with respect to the surface.^{79,80} An orientation order parameter^{53,55,56} was calculated from the difference between the Fe surface normal direction and the direction normal to the plane of the anion ring, as illustrated in Figure S5. The value of orientation order parameter can vary from −0.5 when the anion ring is parallel to the surface to 1 when the anion ring is perpendicular to the surface. The distributions of the orientation order parameter for anions within 5 Å of the substrate (cutoff distance identified from the first peak of the anion position distribution functions, shown in Figure S6) were calculated from the last 1 ns of all three independent simulations for each anion. The results for the [P6,6,6,14] cation are shown in Figure 9, although similar distributions were found for other cations, as shown in Figure

S7 for [P4,4,4,4]. It can be seen that more of the [Benz] anions have an orientation order parameter near 1, meaning they are perpendicular to the surface, whereas the orientation order parameter for the [Sacc] anions is lower, indicating fewer are perpendicular. It has been reported that all three anions can orient perpendicular to metal surfaces,^{81–85} but the asymmetry of the [Sacc] anion causes it to tilt toward the surface.⁸⁵ The preferred perpendicular alignment of the [Benz] anions allows the cations more access to the surface, consistent with the stronger Fe–cation adhesion for the [Benz] ILs than the [Sacc] ILs in Figure 8b.

The cohesive energy between the cation P atoms and the anions is plotted vs anion in Figure 10a. The results show that the cohesion was strongest for [Sacc] and weakest for [Benz] with any cation. This trend was explained by the average distance between the cation P atom and the COM of the nearest anion, in Figure 10b, that increased as [Sacc] < [Sali] < [Benz]. As presented in Figure S8, there are more atoms in [Sacc] that have attractive interactions with the cation than the other two anions, and the extra O atom in [Sali] enables stronger cohesion than [Benz]. The cohesion energy and distance trends are consistent with the contact angle results.

CONCLUSIONS

The wetting of phosphonium ILs with systematically varied cation and anion combinations on ferrous surfaces was evaluated using experiments and MD simulations. Contact angles of less than 20° in experiments indicated that the ILs have a good wettability on stainless steel, but contact angles are different for [Benz], [Sali], and [Sacc]. The same trend was reproduced in MD simulations. Next, the simulations were extended to include five different cations [P4,4,4,4], [P4,4,4,8], [P4,4,4,14], [P6,6,6,14], and [P8,8,8,14] in combination with the three anions. It was found that longer alkyl chains in the cations led to lower contact angles. This was explained by the effect of more C atoms that both increased adhesion with the substrate and separated the P atom in the cation from the anion, thereby decreasing cohesion. For anions, the contact angle increased as [Benz] < [Sali] < [Sacc] when paired with

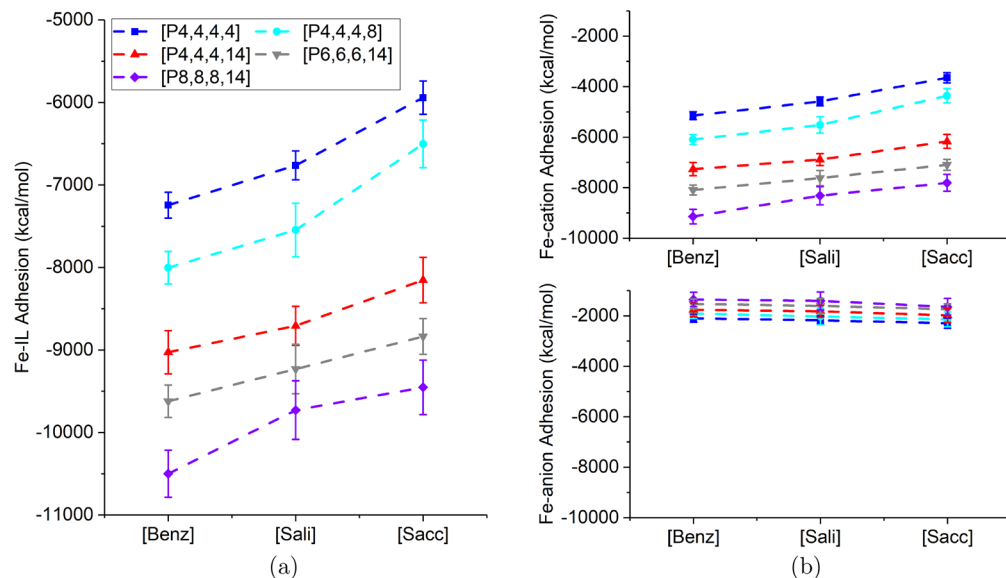


Figure 8. (a) Adhesive interaction energy between the surface and the ILs and (b) separated into the cation (top) and anion (bottom) contributions plotted vs anion for the five cations. Note that this is the same data as in Figure 5 but plotted vs anion to illustrate anion trends.

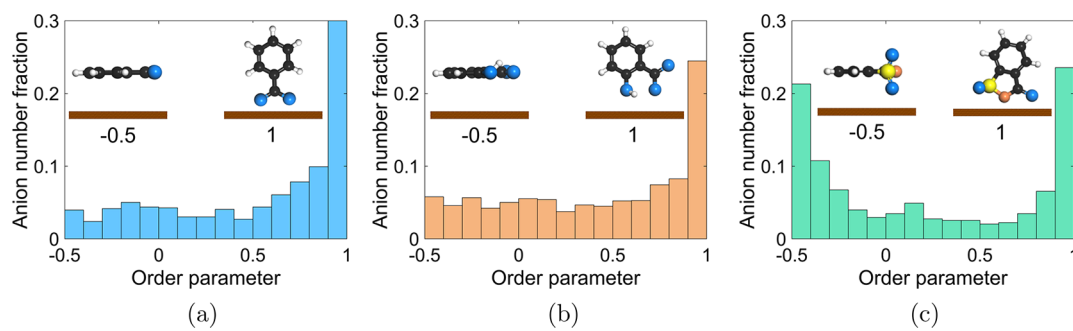


Figure 9. Orientation order parameter distribution for (a) [Benz], (b) [Sali], and (c) [Sacc] paired with [P6,6,6,14] calculated from the last 1 ns of three independent simulations for each anion. Parameter ranges from -0.5 when the anion ring is parallel to the surface to 1 when the anion ring is perpendicular to the surface.

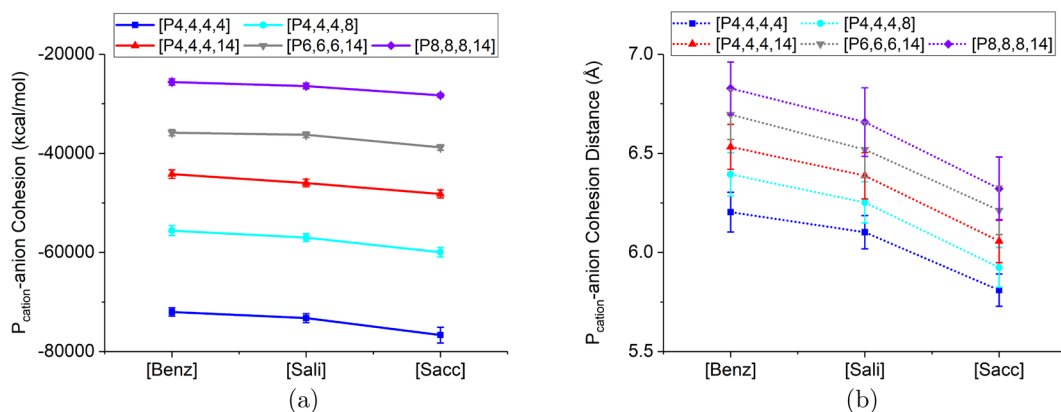


Figure 10. (a) Cohesive energy between P atoms in the cations and all atoms in the anions, and (b) average distance between cation P atoms and the COM of the anions plotted vs anions for the five cations. Note that this is the same data as in Figure 6 but plotted vs anion to illustrate anion trends.

the same cation. Like the cations, the anion contact angle trend was consistent with cohesion energy and explained by the number and type of atoms in the anions that had attractive interactions with the P atom in the cations. The adhesion energy was also consistent with the anion contact angle trend, but this case was explained by the orientation of the anions with respect to the surface. Specifically, perpendicular anion alignment allowed the cations more access to the surface, thereby increasing adhesion. The alignment trends were associated with the asymmetry of the anion structures, where greater symmetry led to more perpendicular alignment, higher cation–Fe adhesion, and a lower contact angle.

Overall, the results reported here demonstrate that both the cation and the anion affect the contact angle through their direct and indirect influence on adhesion and cohesion. Although this study focused on the ions, the simulation-based methods developed may be extended in future work to explore the effects of surface parameters and operating conditions. Also, simulation results for more combinations of cations and anions might be used to develop analytical relationships between the IL properties and the contact angle. Together with matched experiments, such simulations can provide fundamental understanding of the mechanisms underlying the wettability of ILs.

ASSOCIATED CONTENT

Supporting Information

The Supporting Information is available free of charge at <https://pubs.acs.org/doi/10.1021/acs.jpcb.2c01989>.

Additional analysis from MD simulations; contents include a schematic and detailed explanation of the contact angle calculation, Fe–cation adhesion interaction energy by atom type, $C_{\text{cation}}\text{–anion}$ and $P_{\text{cation}}\text{–anion}$ cohesion interaction energy, Fe–anion adhesion interaction energy by atom type, illustration and description of the orientation order parameter calculation, Fe–anion vertical distance distribution, anion orientation order parameter distribution, and $P_{\text{cation}}\text{–anion}$ cohesion interaction energy by atom type (PDF)

AUTHOR INFORMATION

Corresponding Author

Ashlie Martini – Department of Mechanical Engineering, University of California Merced, Merced, California 95343, United States; orcid.org/0000-0003-2017-6081; Phone: (209) 228-2354; Email: amartini@ucmerced.edu

Authors

Ting Liu – Department of Mechanical Engineering, University of California Merced, Merced, California 95343, United States

Md Hafizur Rahman – Department of Mechanical Engineering, University of Nevada Reno, Reno, Nevada 89557, United States

Pradeep L. Menezes – Department of Mechanical Engineering, University of Nevada Reno, Reno, Nevada 89557, United States; orcid.org/0000-0001-9977-6797

Complete contact information is available at:

<https://pubs.acs.org/10.1021/acs.jpcb.2c01989>

Notes

The authors declare no competing financial interest.

ACKNOWLEDGMENTS

The authors acknowledge the support of the National Science Foundation (Grant Nos. CMMI-2010205 and 2010584). The authors also appreciate valuable input from Dr. Manish Patel.

IONIC LIQUID ABBREVIATIONS

BMIM	1-butyl-3-methylimidazolium
DMIM	1,3-dimethylimidazolium tetrafluoroborate
EMIM	1-ethyl-3-methylimidazolium
PrMIM	1-propyl-3-methylimidazolium
P4,4,4,4	tetrabutylphosphonium
P4,4,4,8	tributyloctylphosphonium
P4,4,4,14	tributyltetradecylphosphonium
P6,6,6,14	trihexyltetradecylphosphonium
P8,8,8,14	trioctyltetradecylphosphonium
(iC ₈) ₂ PO ₂	bis(2,4,4-trimethylpentyl) phosphinate
BEHP	bis(2-ethylhexyl)phosphate
Benz	benzoate
BF ₄	tetrafluoroborate
Br	bromide
Cl	chloride
Cpy	2-cyanopyrrolide
DCA	dicyanamide
DEP	diethyl phosphate
PF ₆	hexafluorophosphate
PTFE	poly(tetrafluoroethylene)
p-TsO	p-toluene-sulfonate
Sacc	saccharinate
Sali	salicylate
Tf ₂ N	bis(trifluoromethylsulfonyl)amide

REFERENCES

- (1) Singh, S. K.; Savoy, A. W. Ionic liquids synthesis and applications: An overview. *J. Mol. Liq.* **2020**, *297*, 112038.
- (2) Joshi, M. D.; Anderson, J. L. Recent advances of ionic liquids in separation science and mass spectrometry. *RSC Adv.* **2012**, *2*, 5470–5484.
- (3) Reeves, C. J.; Siddaiah, A.; Menezes, P. L. Ionic liquids: a plausible future of bio-lubricants. *J. Bio. Trib. Corros.* **2017**, *3*, 18.
- (4) Welton, T. Ionic liquids: a brief history. *Biophys. Rev.* **2018**, *10*, 691–706.
- (5) Rahman, M. H.; Khajeh, A.; Panwar, P.; Patel, M.; Martini, A.; Menezes, P. L. Recent progress on phosphonium-based room temperature ionic liquids: Synthesis, properties, tribological performances and applications. *Tribol. Int.* **2022**, *167*, 107331.
- (6) Koutsoukos, S.; Philipp, F.; Malaret, F.; Welton, T. A review on machine learning algorithms for the ionic liquid chemical space. *Chem. Sci.* **2021**, *12*, 6820–6843.
- (7) Moniruzzaman, M.; Kamiya, N.; Goto, M. Activation and stabilization of enzymes in ionic liquids. *Org. Biomol. Chem.* **2010**, *8*, 2887–2899.
- (8) Scarbath-Evers, L. K.; Hunt, P. A.; Kirchner, B.; MacFarlane, D. R.; Zahn, S. Molecular features contributing to the lower viscosity of phosphonium ionic liquids compared to their ammonium analogues. *Phys. Chem. Chem. Phys.* **2015**, *17*, 20205–20216.
- (9) Naik, P. K.; Paul, S.; Banerjee, T. Physicochemical properties and molecular dynamics simulations of phosphonium and ammonium based deep eutectic solvents. *J. Solution Chem.* **2019**, *48*, 1046–1065.
- (10) Maton, C.; de Vos, N.; Stevens, C. V. Ionic liquid thermal stabilities: decomposition mechanisms and analysis tools. *Chem. Soc. Rev.* **2013**, *42*, 5963–5977.
- (11) Khajeh, A.; Rahman, M. H.; Liu, T.; Panwar, P.; Menezes, P. L.; Martini, A. Thermal decomposition of phosphonium salicylate and phosphonium benzoate ionic liquids. *J. Mol. Liq.* **2022**, *352*, 118700.
- (12) Yu, B.; Bansal, D. G.; Qu, J.; Sun, X.; Luo, H.; Dai, S.; Blau, P. J.; Bunting, B. G.; Mordukhovich, G.; Smolenski, D. J. Oil-miscible and non-corrosive phosphonium-based ionic liquids as candidate lubricant additives. *Wear* **2012**, *289*, 58–64.
- (13) Cai, M.; Yu, Q.; Liu, W.; Zhou, F. Ionic liquid lubricants: When chemistry meets tribology. *Chem. Soc. Rev.* **2020**, *49*, 7753–7818.
- (14) Henriques, R. R.; Soares, B. G. Sepiolite modified with phosphonium ionic liquids as anticorrosive pigment for epoxy coatings. *Appl. Clay Sci.* **2021**, *200*, 105890.
- (15) Shah, F. U.; Glavatskikh, S.; MacFarlane, D. R.; Somers, A.; Forsyth, M.; Antzutkin, O. N. Novel halogen-free chelated orthoborate-phosphonium ionic liquids: synthesis and tribophysical properties. *Phys. Chem. Chem. Phys.* **2011**, *13*, 12865–12873.
- (16) Totolin, V.; Minami, I.; Gabler, C.; Dörr, N. Halogen-free borate ionic liquids as novel lubricants for tribological applications. *Tribol. Int.* **2013**, *67*, 191–198.
- (17) Zhu, L.; Dong, J.; Ma, Y.; Jia, Y.; Peng, C.; Li, W.; Zhang, M.; Gong, K.; Wang, X. Synthesis and investigation of halogen-free phosphonium-based ionic liquids for lubrication applications. *Tribol. Trans.* **2019**, *62*, 943–954.
- (18) Sydow, M.; Owsiania, M.; Franski, G.; Woźniak-Karczewska, M.; Piotrowska-Cyplik, A.; Ławniczak, Ł; Szulc, A.; Zgoła-Grzeskowiak, A.; Heipieper, H. J.; Chrzanowski, Ł. Biodiversity of soil bacteria exposed to sub-lethal concentrations of phosphonium-based ionic liquids: Effects of toxicity and biodegradation. *Ecotoxicol. Environ. Saf.* **2018**, *147*, 157–164.
- (19) Oulego, P.; Blanco, D.; Ramos, D.; Viesca, J. L.; Diaz, M.; Hernandez Battez, A. Environmental properties of phosphonium, imidazolium and ammonium cation-based ionic liquids as potential lubricant additives. *J. Mol. Liq.* **2018**, *272*, 937–947.
- (20) Rohlmann, P.; Munavirov, B.; Furó, I.; Antzutkin, O.; Rutland, M. W.; Glavatskikh, S. Non-halogenated ionic liquid dramatically enhances tribological performance of biodegradable oils. *Front. Chem.* **2019**, *7*, 98.
- (21) Yu, G.; Yan, S.; Zhou, F.; Liu, X.; Liu, W.; Liang, Y. Synthesis of cationic symmetrical and asymmetrical ionic liquids and their tribological properties as ultrathin films. *Tribol. Lett.* **2007**, *25*, 197–205.
- (22) Grace, J.; Vysochanska, S.; Lodge, J.; Iglesias, P. Ionic liquids as additives of coffee bean oil in steel-steel contacts. *Lubricants* **2015**, *3*, 637–649.
- (23) Zhou, Y.; Qu, J. Ionic liquids as lubricant additives: a review. *ACS Appl. Mater. Interfaces* **2017**, *9*, 3209–3222.
- (24) Reeves, C. J.; Siddaiah, A.; Menezes, P. L. Tribological study of imidazolium and phosphonium ionic liquid-based lubricants as additives in carboxylic acid-based natural oil: advancements in environmentally friendly lubricants. *J. Cleaner Prod.* **2018**, *176*, 241–250.
- (25) Yang, J.; Zhou, Z.; Liang, Y.; Tang, J.; Gao, Y.; Niu, J.; Dong, H.; Tang, R.; Tang, G.; Cao, Y. Sustainable Preparation of Microcapsules with Desirable Stability and Bioactivity Using Phosphonium Ionic Liquid as a Functional Additive. *ACS Sustainable Chem. Eng.* **2020**, *8*, 13440–13448.
- (26) Reeves, C. J.; Kasar, A. K.; Menezes, P. L. Tribological performance of environmental friendly ionic liquids for high-temperature applications. *J. Cleaner Prod.* **2021**, *279*, 123666.
- (27) Tsunashima, K.; Sugiyama, M. Physical and electrochemical properties of low-viscosity phosphonium ionic liquids as potential electrolytes. *Electrochim. Commun.* **2007**, *9*, 2353–2358.
- (28) Girard, G. M.; Hilder, M.; Zhu, H.; Nucciarone, D.; Whitbread, K.; Zavorine, S.; Moser, M.; Forsyth, M.; MacFarlane, D. R.; Howlett, P. C. Electrochemical and physicochemical properties of small

phosphonium cation ionic liquid electrolytes with high lithium salt content. *Phys. Chem. Chem. Phys.* **2015**, *17*, 8706–8713.

(29) Chen, F.; Kerr, R.; Forsyth, M. Cation effect on small phosphonium based ionic liquid electrolytes with high concentrations of lithium salt. *J. Chem. Phys.* **2018**, *148*, 193813.

(30) Meikandan, M.; Ganesh Kumar, P.; Sundarraj, M.; Yogaraj, D. Numerical analysis on heat transfer characteristics of ionic liquids in a tubular heat exchanger. *Int. J. Ambient Energy* **2020**, *41*, 911–917.

(31) Thasneema, K.; Thayyil, M. S.; Rosalin, T.; Elyas, K.; Dipin, T.; Sahu, P. K.; Krishna Kumar, N. K.; Saheer, V.; Messali, M.; Hadda, T. B. Thermal and spectroscopic investigations on three phosphonium based ionic liquids for industrial and biological applications. *J. Mol. Liq.* **2020**, *307*, 112960.

(32) Tindale, J. J.; Ragogna, P. J. Highly fluorinated phosphonium ionic liquids: novel media for the generation of superhydrophobic coatings. *Chem. Commun.* **2009**, 1831–1833.

(33) Tindale, J.; Mouland, K.; Ragogna, P. Thiol appended, fluorinated phosphonium ionic liquids as covalent superhydrophobic coatings. *J. Mol. Liq.* **2010**, *152*, 14–18.

(34) Dias, A. M.; Marceneiro, S.; Braga, M. E.; Coelho, J. F.; Ferreira, A. G.; Simões, P. N.; Veiga, H. I.; Tomé, L. C.; Marrucho, I. C.; Esperança, J. M.; et al. Phosphonium-based ionic liquids as modifiers for biomedical grade poly (vinyl chloride). *Acta Biomater.* **2012**, *8*, 1366–1379.

(35) Nguyen, T. K. L.; Livi, S.; Pruvost, S.; Soares, B. G.; Duchet-Rumeau, J. Ionic liquids as reactive additives for the preparation and modification of epoxy networks. *J. Polym. Sci., Part A: Polym. Chem.* **2014**, *52*, 3463–3471.

(36) Youssi, M.; Livi, S.; Duchet-Rumeau, J. Ionic liquids: A new way for the compatibilization of thermoplastic blends. *Chem. Eng. J.* **2014**, *255*, 513–524.

(37) Lins, L. C.; Livi, S.; Duchet-Rumeau, J.; Gérard, J.-F. Phosphonium ionic liquids as new compatibilizing agents of biopolymer blends composed of poly (butylene-adipate-co-terephthalate)/poly (lactic acid)(PBAT/PLA). *RSC Adv.* **2015**, *5*, 59082–59092.

(38) Soares, B. G.; Silva, A. A.; Pereira, J.; Livi, S. Preparation of epoxy/Jeffamine networks modified with phosphonium based ionic liquids. *Macromol. Mater. Eng.* **2015**, *300*, 312–319.

(39) Westerholt, A.; Weschta, M.; Bosmann, A.; Tremmel, S.; Korth, Y.; Wolf, M.; Schlucker, E.; Wehrum, N.; Lennert, A.; Uerdingen, M.; et al. synthesis and tribological performance of oil-miscible ammonium and phosphonium-based ionic liquids. *ACS Sustainable Chem. Eng.* **2015**, *3*, 797–808.

(40) Blanco, D.; Bartolome, M.; Ramajo, B.; Viesca, J.; Gonzalez, R.; Hernandez Battez, A. Wetting properties of seven phosphonium cation-based ionic liquids. *Ind. Eng. Chem. Res.* **2016**, *55*, 9594–9602.

(41) Batchelor, T.; Cunder, J.; Fadeev, A. Y. Wetting study of imidazolium ionic liquids. *J. Colloid Interface Sci.* **2009**, *330*, 415–420.

(42) Pameijer, C. H.; Glantz, P.-O.; von Fraunhofer, A. Clinical and Technical Considerations of Luting Agents for Fixed Prosthodontics. *Int. J. Dent.* **2012**, *2012*, 565303.

(43) Kalin, M.; Polajnar, M. The effect of wetting and surface energy on the friction and slip in oil-lubricated contacts. *Tribol. Lett.* **2013**, *52*, 185–194.

(44) Liu, T.; Wang, K.; Chen, Y.; Zhao, S.; Han, Y. Dominant role of wettability in improving the specific capacitance. *Green Energy Environ.* **2019**, *4*, 171–179.

(45) Grundke, K.; Bogumil, T.; Werner, C.; Janke, A.; Pöschel, K.; Jacobasch, H.-J. Liquid-fluid contact angle measurements on hydrophilic cellulosic materials. *Colloids Surf., A* **1996**, *116*, 79–91.

(46) Uelzen, T.; Müller, J. Wettability enhancement by rough surfaces generated by thin film technology. *Thin Solid Films* **2003**, *434*, 311–315.

(47) Matczak, L.; Johanning, C.; Gil, E.; Guo, H.; Smith, T. W.; Schertzer, M.; Iglesias, P. Effect of cation nature on the lubricating and physicochemical properties of three ionic liquids. *Tribol. Int.* **2018**, *124*, 23–33.

(48) Zhang, W.; Jiang, S.; Sun, J.; Wu, Z.; Qin, T.; Xi, X. Wettability of coal by room temperature ionic liquids. *Int. J. Coal Prep. Util.* **2021**, *41*, 418–427.

(49) Tiago, G.; Restolho, J.; Forte, A.; Colaço, R.; Branco, L.; Saramago, B. Novel ionic liquids for interfacial and tribological applications. *Colloids Surf., A* **2015**, *472*, 1–8.

(50) Carrera, G. V.; Afonso, C. A.; Branco, L. C. Interfacial properties, densities, and contact angles of task specific ionic liquids. *J. Chem. Eng. Data* **2010**, *55*, 609–615.

(51) Cigno, E.; Magagnoli, C.; Pierce, M. S.; Iglesias, P. Lubricating ability of two phosphonium-based ionic liquids as additives of a bio-oil for use in wind turbines gearboxes. *Wear* **2017**, *376*, 756–765.

(52) Zhao, X.; Zhu, Y.; Zhang, C.; Lei, J.; Ma, Y.; Du, F. Positive charge pesticide nanoemulsions prepared by the phase inversion composition method with ionic liquids. *RSC Adv.* **2017**, *7*, 48586–48596.

(53) Malali, S.; Foroutan, M. Study of wetting behavior of BMIM./PF6-ionic liquid on TiO₂ (110) surface by molecular dynamics simulation. *J. Phys. Chem. C* **2017**, *121*, 11226–11233.

(54) Bordes, E.; Douce, L.; Quitevis, E. L.; Pádua, A. A.; Costa Gomes, M. Ionic liquids at the surface of graphite: Wettability and structure. *J. Chem. Phys.* **2018**, *148*, 193840.

(55) Bhattacharjee, S.; Khan, S. Effect of alkyl chain length on the wetting behavior of imidazolium based ionic liquids: A molecular dynamics study. *Fluid Phase Equilib.* **2019**, *501*, 112253.

(56) Bhattacharjee, S.; Khan, S. The wetting behavior of aqueous imidazolium based ionic liquids: a molecular dynamics study. *Phys. Chem. Chem. Phys.* **2020**, *22*, 8595–8605.

(57) Atkinson, H.; Bara, J. E.; Turner, C. H. Molecular-level analysis of the wetting behavior of imidazolium-based ionic liquids on bismuth telluride surfaces. *Chem. Eng. Sci.* **2020**, *211*, 115270.

(58) Bahrami, M.; Ghatee, M. H.; Ayatollahi, S. F. Simulation of Wetting and Interfacial Behavior of Quaternary Ammonium and Phosphonium Ionic Liquid Nanodroplets Over Face-Centered Cubic Metal Surfaces. *J. Phys. Chem. B* **2020**, *124*, 2835–2847.

(59) Castejon, H. J.; Wynn, T. J.; Marcin, Z. M. Wetting and tribological properties of ionic liquids. *J. Phys. Chem. B* **2014**, *118*, 3661–3668.

(60) Liu, H.; Jiang, L. Wettability by ionic liquids. *Small* **2016**, *12*, 9–15.

(61) Manoj, A.; Kasar, A. K.; Menezes, P. L. Tribocorrosion of porous titanium used in biomedical applications. *J. Bio. Trib. Corros.* **2019**, *5*, 3.

(62) Egorov, V. M.; Djigailo, D. I.; Momotenko, D. S.; Chernyshov, D. V.; Torocheshnikova, I. I.; Smirnova, S. V.; Pletnev, I. V. Task-specific ionic liquid trioctylmethylammonium salicylate as extraction solvent for transition metal ions. *Talanta* **2010**, *80*, 1177–1182.

(63) Kasar, A. K.; Reeves, C. J.; Menezes, P. L. The effect of particulate additive mixtures on the tribological performance of phosphonium-based ionic liquid lubricants. *Tribol. Int.* **2022**, *165*, 107300.

(64) Jorgensen, W. L.; Maxwell, D. S.; Tirado-Rives, J. Development and testing of the OPLS all-atom force field on conformational energetics and properties of organic liquids. *J. Am. Chem. Soc.* **1996**, *118*, 11225–11236.

(65) Dodd, L. S.; Cabeza de Vaca, I.; Tirado-Rives, J.; Jorgensen, W. L. LigParGen web server: an automatic OPLS-AA parameter generator for organic ligands. *Nucleic Acids Res.* **2017**, *45*, W331–W336.

(66) Maghfiroh, C.; Arkundato, A.; Maulina, W.; et al. Parameters (σ , ϵ) of Lennard-Jones for Fe, Ni, Pb for Potential and Cr based on Melting Point Values Using the Molecular Dynamics Method of the Lammps Program. *J. Phys.: Conf. Ser.* **2020**, 012022.

(67) Delhommele, J.; Millié, P. Inadequacy of the Lorentz-Berthelot combining rules for accurate predictions of equilibrium properties by molecular simulation. *Mol. Phys.* **2001**, *99*, 619–625.

(68) Herrera, C.; Garcia, G.; Atilhan, M.; Aparicio, S. Nanowetting of graphene by ionic liquid droplets. *J. Phys. Chem. C* **2015**, *119*, 24529–24537.

(69) Burt, R.; Birkett, G.; Salanne, M.; Zhao, X. Molecular dynamics simulations of the influence of drop size and surface potential on the contact angle of ionic-liquid droplets. *J. Phys. Chem. C* **2016**, *120*, 15244–15250.

(70) Guan, Y.; Shao, Q.; Chen, W.; Liu, S.; Zhang, X.; Deng, Y. Dynamic three-dimensional nanowetting behavior of imidazolium-based ionic liquids probed by molecular dynamics simulation. *J. Phys. Chem. C* **2017**, *121*, 23716–23726.

(71) Martínez, L.; Andrade, R.; Birgin, E. G.; Martínez, J. M. PACKMOL: a package for building initial configurations for molecular dynamics simulations. *J. Comput. Chem.* **2009**, *30*, 2157–2164.

(72) Plimpton, S. Fast parallel algorithms for short-range molecular dynamics. *J. Comput. Phys.* **1995**, *117*, 1–19.

(73) Evans, D. J.; Holian, B. L. The Nose–Hoover thermostat. *J. Comput. Phys.* **1985**, *83*, 4069–4074.

(74) Spreiter, Q.; Walter, M. Classical molecular dynamics simulation with the Velocity Verlet algorithm at strong external magnetic fields. *J. Comput. Phys.* **1999**, *152*, 102–119.

(75) Santiso, E. E.; Herdes, C.; Müller, E. A. On the calculation of solid-fluid contact angles from molecular dynamics. *Entropy* **2013**, *15*, 3734–3745.

(76) Khalkhali, M.; Kazemi, N.; Zhang, H.; Liu, Q. Wetting at the nanoscale: A molecular dynamics study. *J. Chem. Phys.* **2017**, *146*, 114704.

(77) Yuan, Y.; Lee, T. R. In *Surface Science Techniques*; Bracco, G., Holst, B., Eds.; Springer Berlin Heidelberg: Berlin, Heidelberg, 2013; pp 3–34.

(78) Liu, F.; Shen, W. Forced wetting and dewetting of liquids on solid surfaces and their roles in offset printing. *Colloids Surf., A* **2008**, *316*, 62–69.

(79) Aliaga, C.; Baldelli, S. A sum frequency generation study of the room-temperature ionic liquid–titanium dioxide interface. *J. Phys. Chem. C* **2008**, *112*, 3064–3072.

(80) Xu, S.; Xing, S.; Pei, S.-S.; Baldelli, S. Sum frequency generation spectroscopy study of an ionic liquid at a graphene-BaF₂ (111) interface. *J. Phys. Chem. B* **2014**, *118*, 5203–5210.

(81) Guo, Q.; Cocks, I.; Williams, E. The adsorption of benzoic acid on a TiO₂ (110) surface studied using STM, ESDIAD and LEED. *Surf. Sci.* **1997**, *393*, 1–11.

(82) Perry, C.; Haq, S.; Frederick, B.; Richardson, N. Face specificity and the role of metal adatoms in molecular reorientation at surfaces. *Surf. Sci.* **1998**, *409*, 512–520.

(83) Frederick, B.; Leibsle, F.; Haq, S.; Richardson, N. Evolution of lateral order and molecular reorientation in the benzoate/Cu (110) system. *Surf. Rev. Lett.* **1996**, *3*, 1523–1546.

(84) Morosanova, M. A.; Morosanova, E. I. Silica-titania xerogel for solid phase spectrophotometric determination of salicylate and its derivatives in biological liquids and pharmaceuticals. *Chem. Cent. J.* **2015**, *9*, 64.

(85) Imai, Y.; Kamada, J.-i. Vibrational spectra of saccharin nitranion and its orientation on the surface of silver metal particles. *Spectrochim. Acta, Part A* **2005**, *61*, 711–715.